

# PCCP

Accepted Manuscript



This is an *Accepted Manuscript*, which has been through the Royal Society of Chemistry peer review process and has been accepted for publication.

*Accepted Manuscripts* are published online shortly after acceptance, before technical editing, formatting and proof reading. Using this free service, authors can make their results available to the community, in citable form, before we publish the edited article. We will replace this *Accepted Manuscript* with the edited and formatted *Advance Article* as soon as it is available.

You can find more information about *Accepted Manuscripts* in the [Information for Authors](#).

Please note that technical editing may introduce minor changes to the text and/or graphics, which may alter content. The journal's standard [Terms & Conditions](#) and the [Ethical guidelines](#) still apply. In no event shall the Royal Society of Chemistry be held responsible for any errors or omissions in this *Accepted Manuscript* or any consequences arising from the use of any information it contains.

## The Role of Electronic Energy Loss on Irradiation-Induced Grain Growth in Nanocrystalline Oxides

Yanwen Zhang,<sup>1,2,\*</sup> Dilpuneet S. Aidhy,<sup>1</sup> Tamas Varga,<sup>3</sup> Sandra Moll,<sup>4</sup> Philip D. Edmondson,<sup>5</sup> Fereydoon Namavar,<sup>6</sup> Ke Jin,<sup>2</sup> Christopher N. Ostrouchov,<sup>2</sup> and William J. Weber<sup>2,1</sup>

<sup>1</sup>*Materials Science & Technology Division, Oak Ridge National Laboratory, Oak Ridge, TN 37831, USA*

<sup>2</sup>*Department of Materials Science & Engineering, University of Tennessee, Knoxville, TN 37996, USA*

<sup>3</sup>*Pacific Northwest National Laboratory, PO Box 999, Richland, WA 99352, USA*

<sup>4</sup>*TN International / AREVA, 1, rue des Hérons, 78182 Montigny Le Bretonneux, France*

<sup>5</sup>*Department of Materials, University of Oxford, Parks Road, Oxford OX1 3PH, UK*

<sup>6</sup>*University of Nebraska Medical Center, Omaha, NE 68198, USA*

Grain growth of nanocrystalline materials is generally thermally activated, but can also be driven by irradiation at much lower temperature. In nanocrystalline ceria and zirconia, energetic ions deposit their energy to both atomic nuclei and electrons. Our experimental results have shown that irradiation-induced grain growth is dependent on the total energy deposited, where electronic energy loss and elastic collisions between atomic nuclei both contribute to the production of disorder and grain growth. Our atomistic simulations reveal that a high density of disorder near grain boundaries leads to locally rapid grain movement. The additive effect from both electronic excitation and atomic collision cascades on grain growth demonstrated in this work opens up new possibilities for controlling grain sizes to improve functionality of nanocrystalline materials.

Keywords: nanocrystalline ceramic; ion irradiation; disorder; energy loss; grain boundary;

\* To whom correspondence should be addressed: Oak Ridge National Laboratory, 4500S (A148), MS 6138, Oak Ridge, Tennessee 37831-6138; Email: [Zhangy1@ornl.gov](mailto:Zhangy1@ornl.gov)

## 1. Introduction

With advances in nanotechnology, nanostructured materials with grain sizes well below 100 nm are attracting interest for a wide variety of applications, including novel catalyst, sensors, electronics, membranes, drug delivery, coatings, batteries, solar cells, fuel cells, and advanced nuclear energy systems.<sup>[1-10]</sup> Ceramics are key engineering materials for electronic, optical, space and nuclear industries, and nanostructured oxides are considered as potential candidates in advanced energy storage and production.<sup>[10]</sup> Ceria ( $\text{CeO}_2$ ) has a stable fluorite-structure that does not show any known crystallographic change from room temperature up to its melting point ( $\sim 2700$  °C). As an exceptional mixed electronic-ionic conductor,<sup>[1,11]</sup> the properties of  $\text{CeO}_2$  strongly depend upon its microstructure, temperature, and the ambient oxygen activity. Zirconia ( $\text{ZrO}_2$ ) has been well studied due to its superior chemical, mechanical and optical properties. While pure  $\text{ZrO}_2$  has a monoclinic crystal structure at room temperature and reversibly transforms to tetragonal and cubic phases at high temperatures, cubic phase  $\text{ZrO}_2$  with nanoscale dimensions is proven to be stable at room temperature<sup>[5,12,13]</sup> The tetragonal and cubic phases have attracted the most attention as various coating materials, refractory materials, and dispersed phases in composite materials.

In the context of nuclear fuels and the transmutation of radioactive actinides, cubic  $\text{ZrO}_2$  and  $\text{CeO}_2$ , which are isostructural with  $\text{UO}_2$ ,  $\text{ThO}_2$  and  $\text{PuO}_2$ , have been used as model systems for evaluating the performance of nuclear fuel and inert matrices in harsh radiation environments. Ever increasing energy needs and the disaster at Fukushima nuclear power plants have raised the demands for advanced fuels and cladding materials that withstand irradiation for longer periods of time with improved accident tolerance. Nanostructured ceramic materials may provide improved operational fuel performance and better response in loss of coolant accidents in terms of enhanced radiation resistance, improved mechanical strength, reduced cracking and higher thermal conductivity due to the high density of interfaces and grain boundaries (GBs). Knowledge on the response of nanograined oxides to irradiation is essential to successful utilization of the materials in a radiation environment. Moreover, ion beams provide an effective approach to tailor size-dependent material properties of oxide-based nanomaterials.

The ability to control and engineer materials by ion beams in a far from equilibrium environment, which is different from conventional thermal equilibrium processing, may have profound impacts for research on new clean energy sources, sensors, and high energy density batteries.

To understand ion-induced electronic and atomic processes on microstructure evolution, ion irradiation studies in nanocrystalline CeO<sub>2</sub> and ZrO<sub>2</sub> are performed using high energy Si and Au ions to evaluate the structural response to different electronic and nuclear energy deposition, as well as the different ratio of electronic to nuclear energy deposition. The structural response to ion-energy deposition is investigated and discussed with a focus on the impact from both electronic and atomic processes, as well as the coupled dynamics. Our experimental results reveal that both electronic energy loss and nuclear energy loss contribute to grain growth; our atomistic simulations demonstrate that adding high levels of local disorder, as would be expected from ion-solid interactions, leads to rapid grain growth, consistent with our experimental results. The additive effects of electronic excitation and atomic collision cascades on grain growth in nanocrystalline ceria and zirconia films have not been reported previously, and these mechanisms provide a pathway to control defects and tailor grain size in nanocrystalline materials.

## 2. Experiments and Simulation Conditions

Nanocrystalline CeO<sub>2</sub> (~ 250 to 350 nm) and ZrO<sub>2</sub> (~ 460 nm) films with an average grain size from ~ 5.5 to 10 nm were deposited on a Si(100) wafer using an ion beam assisted deposition (IBAD) technique (Mill Lane Engineering, Lowell, MA) at room temperature.<sup>[5]</sup> The ceria films were subjected to 1.0 MeV Si and 3.0 MeV Au ion irradiations at room temperature at fluences up to  $\sim 3.49 \times 10^{16}$  and  $\sim 1.9 \times 10^{16}$  cm<sup>-2</sup>, respectively. To estimate the temperature effect, Au irradiations in CeO<sub>2</sub> were also carried out at 160 K. To differentiate the effects from electronic and nuclear energy losses, ZrO<sub>2</sub> films were irradiated with 3.0 and 12 MeV Au ions at ion fluences up to  $5 \times 10^{15}$  cm<sup>-2</sup> at room temperature with a goal to deposit different amounts of energy to target electrons and atoms by varying the ratio of electronic to nuclear energy loss. For the MeV ions used in this study, the electronic, nuclear and total energy deposition profiles are nearly flat across the oxide films, and most of the Si or Au ions penetrate the films and stop in the Si substrate, resulting in negligible compositional changes. During the irradiation, the ion

beam was rastered over the sample surface with horizontal and vertical scan frequency of 517 and 64 Hz, respectively, to ensure a uniform irradiation.

The Stopping and Range of Ions in Matter (SRIM) code<sup>[14]</sup> is widely used to estimate stopping powers (energy loss) along an ion trajectory in matter. Electronic and nuclear energy losses as a function of depth of the incident ions were determined using the SRIM code under quick damage calculations, while the average dose in displacements per atom (dpa) was estimated under full-cascade simulations. For the Si irradiation in CeO<sub>2</sub>, the sample density of 6.3 g cm<sup>-3</sup> was experimentally determined and used in the SRIM simulations. For the Au irradiation in CeO<sub>2</sub>, a nominal density of 5.355 g cm<sup>-3</sup> (15% reduction from 6.3 g cm<sup>-3</sup>) is used in the SRIM estimation to compensate for the overestimation of Au electronic stopping power,<sup>[15-18]</sup> and for better comparison to the SRIM-estimated energy loss and dpa values for the Si irradiation. For Au irradiation in ZrO<sub>2</sub>, a density of 5.4 g cm<sup>-3</sup> is used.<sup>[12]</sup> In the SRIM simulation, threshold displacement energies of 27 and 56 eV for O and Ce atoms in CeO<sub>2</sub><sup>[19,20]</sup> and 50 eV for O and Zr atoms in ZrO<sub>2</sub> were used,<sup>[12]</sup> respectively. In addition to the electronic and nuclear energy loss values (keV/nm) calculated directly from the SRIM code, the total energy loss to the target electronic system (electron energy loss: the sum of ionization losses by both ions and recoils) and the energy loss to atomic collisions (damage energy: the difference between the energy absorbed by recoils and the ionization loss by recoils) are also determined from the SRIM quick calculations. In other words, the damage energy is defined as the energy consumed in elastic collision events between atoms. It is worth pointing out that high-energy recoils can further excite target electrons and produce additional atomic displacement damage. Their kinetic energy will transfer to both target atoms and electrons, which are further differentiated as the damage energy and electron energy loss, respectively. Accordingly, the electron energy loss is defined as the total electronic energy loss from both ions and energetic recoils. At very low ion energies (< ~ 1 keV/nucleon) where electronic energy loss is negligible, the nuclear energy loss and the damage energy are similar. At very high ion energies (> ~ 1 MeV/nucleon) where nuclear energy loss is negligible, the difference between electronic energy loss by the incident ion and total electron energy loss is small. For MeV ions used in this study, there is a clear difference in these energy loss terms, as

listed in Table 1 for easy comparison. The SRIM predicted damage (dpa) profile is determined from the sum of the predicted cation and anion vacancy concentrations and the replacement events. The average conversion factor of 0.33 and 0.0224 is used to convert ion fluence  $10^{14} \text{ cm}^{-2}$  to ion dose (dpa) for Au and Si irradiations, respectively, in a 300 nm  $\text{CeO}_2$  film.

The as-deposited and irradiated oxide films were characterized by backscattering spectroscopy technique, cross-sectional transmission electron microscope (TEM), selected-area electron diffraction (SAED), and grazing-incidence X-ray diffraction (GIXRD). The elemental composition and film thickness were characterized by Rutherford backscattering spectroscopy (RBS), which was performed using 2.0 MeV  $\text{He}^+$  beam with two Si detectors located at scattering angles of  $150^\circ$  and  $170^\circ$  relative to the incoming beam. Non-Rutherford backscattering (NRBS) measurements were also carried out at  $170^\circ$  with He beam energy varying from 3.01 to 3.05 MeV, which significantly enhances the scattering cross section of O atoms<sup>[21]</sup> to determine possible composition change of O/Ce and O/Zr due to ion bombardments. TEM specimens were prepared by mechanically polishing down to a thickness of 15 - 20  $\mu\text{m}$  using a tripod polishing technique. Mechanical polishing is followed by ion milling in a Gatan precision ion polishing system with decreasing beam energy from 4.5 keV to 3 keV. The specimens were evaluated using a JEOL 2010 transmission electron microscope operating at 200 kV. The diffractometer (Philips X'Pert MPD) operating at 45 kV and 40 mA has a fixed Cu anode ( $\lambda_{\text{K}\alpha} = 1.54187 \text{ \AA}$ ). A Göbel mirror for the incident beam and a 0.27 radian parallel plate collimator for the diffracted beam were used in this study. Glancing angle incidence at a fixed  $\omega = 5^\circ$  was employed to avoid strong diffraction intensities from the substrate Si. Asymmetric scans were performed at  $2\theta = 20^\circ - 100^\circ$  with a step of  $0.05^\circ$  per 40 sec. Data analysis of the XRD patterns was conducted using commercial software JADE (version 8.5) from Materials Data, Inc., PDF4+ database from ICSD, as well as whole-pattern in TOPAS to get a more accurate volume-weighted average crystallite size. Similar trend of the growth behavior are observed from different spectrum analysis. In current work, all the crystallite sizes have been determined from the main diffraction (111) peak in the same way, using pseudo-Voigt profiles. One may note that

grain size determined from GIXRD represents an average size of the coherently diffracting crystallites and may not be the same as the grain size measured from TEM.

Atomistic simulations were utilized to capture GB movement in nanocrystalline CeO<sub>2</sub> within the limited time scale of molecular dynamics (MD) simulations.<sup>[22]</sup> The simulation methods are briefly summarized here, and the details can be found elsewhere.<sup>[22]</sup> In order to capture GB movement on MD time scale, the simulations were performed at elevated temperature of 2500 K with a time-step of 0.5 fs. A point-ion classical interatomic potential developed by Gotte et al.<sup>[23]</sup> was used where the short-range interactions were described by a rigid-ion Buckingham-type potential; the details on the potential's fidelity can be found elsewhere.<sup>[24,25]</sup> The long-range Columbic interactions were evaluated via Wolf's direct 1/r Columbic summation method<sup>[26]</sup> with spherical truncation at the cut-off radius of 10.71 Å. The zero-temperature lattice parameter is the same as the experimental value of  $a_0=5.411$  Å. Voronoi tessellation method<sup>[27]</sup> was used to construct [100] columnar grain structures with different sizes and shapes within a three-dimensional cell, and the grains are filled by placing ions on a rotated fluorite lattice of CeO<sub>2</sub>. In the grain boundary regions, an ion is removed if it is closer to a neighboring ion by 1.5 Å, while maintaining charge neutrality. Misorientation angles between any two grains is larger than or equal to 30° to ensure high-angle grain boundaries. The initial columnar structures produced at T=0 K are equilibrated by gradually raising the temperature to relax the grain boundaries.

### 3. Results and Discussion

#### 3.1 Grain growth under ion irradiation

The as-deposited CeO<sub>2</sub> and ZrO<sub>2</sub> films were characterized using complementary techniques. The results from the RBS and NRBS measurements have confirmed that there is no stoichiometry change of the films within the detection uncertainty. Microstructural changes are investigated by GIXRD and TEM. GIXRD spectra for the as-deposited CeO<sub>2</sub> film and the samples irradiated by 1 MeV Si at 300 K to ion fluences of  $6.36 \times 10^{15}$  cm<sup>-2</sup> (1.4 dpa) and  $3.49 \times 10^{16}$  cm<sup>-2</sup> (7.8 dpa) are shown in Figure 1, which represent the typical spectrum quality under other Si or Au irradiation conditions. The full width at half maximum (FWHM) of the (111) peak from the as-deposited film is marked as dashed arrows that are placed at the

half maximum of all three (111) peaks to show the width change with increase of irradiation. It is evident from the inset that the width of the (111) peaks become narrower with increasing ion fluence, which clearly indicates the growth of the nanocrystalline grains. The irradiation-induced grain growth is determined by fitting the major peaks for each irradiation. The apparent peak shift after irradiation is related to the stress release upon irradiation.<sup>[28]</sup>

The nanograins with high quality boundaries in the nanocrystalline CeO<sub>2</sub> films are clearly visible in the high-resolution TEM images (Figure 2a-c), confirming the presence of randomly-oriented grains. The diffraction patterns and spots shown in insets indicate a typical polycrystalline structure. The high-resolution TEM image (Figure 2a) displays fine grain structure of the as-deposited film with average grain size of ~5.5 nm. The TEM images of the two irradiated samples, by 3 MeV Au to  $\sim 1 \times 10^{14} \text{ cm}^{-2}$  (0.34 or 0.33 dpa) at 160 K (Figure 2b) and 300 K (Figure 2c), are also included for comparison. Compared with the as-deposited film (Figure 2a), a clear irradiation-induced growth is observed (Figure 2b and c). Such grain growth is also supported by the corresponding SAED patterns, shown as insets, which indicate more discrete diffraction spots after irradiation. To better estimate the grain growth behavior, GIXRD was carried out to examine grain growth as a function of ion fluence over a large number of grains. Since the average grain size determined by GIXRD has relatively lower uncertainty than that from the TEM images, the fitted results of the XRD peaks are used in this study for grain size determination. The GIXRD results show a sublinear dependence (Figure 2d) where fast growth is observed at lower fluence and at higher temperature. The temperature dependence is expected, as the reduced grain growth observed at 160 K may suggest decreased atomic mobility at low temperature that suppresses the grain-growth process.

### 3.2 Disorder-driven grain growth

Ions lose energies as a result of the resistance to ion passage in the material. Conventional understanding suggests that damage in materials is produced in two separated regimes of energies: either by energy transfer directly to atomic nuclei (damage energy) at low keV energies, or by energy transfer directly to the electronic system (electron energy loss) at much higher MeV and GeV energies (such as

swift heavy ions).<sup>[29]</sup> In the current study, MeV Si and Au ions deposit significant energy to both the electronic and atomic structures (Table 1), and the influence from the electronic and nuclear energy deposition may not be negligible or separable. We, therefore, evaluate grain growth as a function of energy loss to produce atomic displacements (damage energy), total energy loss to target electrons (electron energy loss), and the total energy deposition (the sum of the two).

Irradiation-induced grain growth has been well observed in metals. More recently, several studies in ceramic-oxides have also been reported.<sup>[12,30,31]</sup> In the absence of irradiation, grain growth is generally attributed to curvature-driven and grain-rotation mechanisms to reduce the grain-boundary curvature, and both mechanisms are thermally activated. In contrast, under irradiation, we observe grain growth at 160 K and 300 K (Figures 1 and 2). Such low temperature grain growth does not follow the conventional thermally-activated mechanisms, as no thermally-induced grain growth occurs at such low temperatures.

Grain growth in nanocrystalline metallic foils has been reported at room temperature under ion irradiation, and explained by direct impact of thermal spikes on grain boundaries.<sup>[32]</sup> In this model, grain-boundary migration occurs by atomic jumps, within the thermal spikes, biased by the local grain-boundary curvature driving. The average grain size with the ion fluence is described by a power law expression of  $D^n - D_0^n = K\phi$ , where  $D_0$  is the initial mean grain diameter,  $\phi$  is ion fluence, and  $K$  is proportional to the grain boundary mobility of the materials and the driving force.<sup>[32]</sup> The constant  $n$  may be an intrinsic parameter depending on the material system and the dominating grain growth mechanisms. Our work on the irradiation-induced grain growth suggests that  $n$  value is 5 for CeO<sub>2</sub> and 6 for ZrO<sub>2</sub>,<sup>[12]</sup> which is different from the value of 2 for thermally activated grain growth<sup>[33]</sup> and 3 for irradiation-induced grain growth in metals<sup>[32]</sup>.

Our recent findings from MD simulations have revealed a new fast disorder-driven grain growth mechanism in ceramics.<sup>[22]</sup> This disorder-driven mechanism leads to grain growth on a much shorter time scale (a few tens of picoseconds) as compared to processes based on curvature-driven or grain-rotation mechanisms (occurring over a few hundreds of picoseconds). This disorder-driven mechanism may lead to the higher  $n$  value in CeO<sub>2</sub> and ZrO<sub>2</sub>, as compared with lower value in metallic systems. The results

from our MD simulations suggest that the disorder-driven mechanism is only active on MD time scales in the presence of a large amount of local disorder.<sup>[22]</sup> The passage of a MeV ion through a solid material represents a strong intrusion that produces a large number of vacancies and interstitials. Since the energy transferred from an ion to an atomic nucleus in a single collision is often many times greater than the binding energy of a few tens of eV, the atom can be displaced from its original site in the lattice. The recoil atom may receive so much energy that it in turn can displace other atoms, creating a cascade of atomic collision events. Eventually, a large number of atoms within the solid are set in motion with energy dissipated as a rapidly quenched thermal spike. This may lead to vacancy and interstitial defects, mixing of grain boundaries, lattice disorder, and other observable changes in the microstructure in the region around the ion path. Although many interstitials and vacancies may be eliminated by close-pair recombination processes, high atomic disorder of more than 60% is observed in single crystalline yttria-stabilized cubic ZrO<sub>2</sub>.<sup>[34]</sup> Dislocation loops and visible tracks are reported to form in CeO<sub>2</sub> for electronic energy deposition above 12 keV/nm,<sup>[35]</sup> which is much higher than values in the present study (Table 1). In CeO<sub>2</sub> thin films, electronic energy deposition leads to enhanced production of defects and lattice disorder,<sup>[36]</sup> and MD simulations of thermal spikes in CeO<sub>2</sub> from electronic energy deposition (0.7 to 1.2 keV/nm) reveal that only disorder is introduced.<sup>[37]</sup> Such irradiation-induced disorder in nanocrystalline materials where the GB density is high may provide a right non-equilibrium environment for defect or disorder-GB interactions to activate the disorder-driven mechanism.

To further demonstrate grain growth induced by disorder and grain size effect, additional MD simulations are carried out in this work. Grain growth behavior is studied in two MD cells (Figure 3) with a damaged central grain (Figure 3a-d for a 4.5 nm initial central grain and Figure 3 e-h for a 6.5 nm grain). In both grains, the same number of Ce Frenkel pairs is initially created with the same local defect density, therefore, the same disordered volume in both cases. In the smaller grain (4.5 nm) where the disorder is close to GBs, the existing defects (Figure 3a: 0ps) trigger additional defects and disordering that occupy the whole grain in a very short time (Figure 3b: 7ps), leading to the activation of the disorder-driven grain growth mechanism. The disordered grain significantly shrinks at 15 ps (Figure 3c) and is completely

consumed by the neighboring grains at 55 ps (Figure 3d), thereby leading to an overall grain growth. For the larger grain size of 6.5 nm (Figure 3e), the grain volume is increased by more than a factor of 2; although the initial number of defects and local defect density (Figure 3e) are the same as those in the smaller grain (Figure 3a), most defect-GB interactions are observed at up-right part of the central grain at 7 ps (Figure 3f). A majority of the defects are annealed inside the grain within 15 ps (Figure 3g), and only limited grain growth is observed at 55 ps (Figure 3h). The MD results (Figure 3) show that, as the grain size increases, the same amount of local disorder will have less interaction with GBs, resulting in less active grain growth. Thus, only when the disorder, introduced within the simulations or experimentally by irradiation, interactions directly with grain boundaries will grain growth occur, and the probability for such interaction decreases with increasing grain size. This process supports the sublinear dependence (reduced slope) displayed by the GIXRD results (Figure 2d), where the grain growth is less effective with increasing grain size. As revealed from these MD results (Figure 3), grain growth under irradiation can be attributed to the disorder-driven mechanism that is triggered by the interaction of irradiation-induced defects and disorder with grain boundaries. We will now discuss the impact of electronic and nuclear energy loss on grain growth.

### 3.3 Dependence on damage energy

To evaluate if the grain growth mainly results from direct displacement cascade collisions, the irradiation-induced growth is plotted as a function of ion fluence and average ion dose (dpa) (Figure 4). While ion fluence is defined as the total number of ions that intersect a unit area in a specific time interval of interest and has units of  $\text{cm}^{-2}$ , ion dose is a term of deposited energy density and, for damage energy, is often given in the unit of dpa. Since the original grain size of the as-deposited films varies from  $\sim 5.5$  to 10 nm, the irradiation-induced change in grain size is used instead of the actual grain size for easy comparison. The results on ion fluence dependence (Figure 4a) suggest that, in terms of a single-ion event, a heavy Au ion is more efficient in producing grain growth than a Si ion. As Au ions are more efficient in producing displacement damage, one would expect faster grain growth under Au irradiation when the grain growth is plotted as a function of ion fluence. However, the more rapid and larger grain growth

observed for the Si irradiation versus the Au case (Figure 4b) is surprising. The ion-solid interactions in CeO<sub>2</sub> are shown by the collision plots (Figure 5) for 1000 Au ions versus 1000 Si ions, where many more displacement collisions are produced from the Au irradiations. The SRIM simulations suggest that for the same ion fluence of  $10^{14} \text{ cm}^{-2}$ , an average of 0.33 and 0.0224 dpa are produced in a 300 nm CeO<sub>2</sub> film under Au and Si irradiations, respectively. High displacement events by Au ions and collision plots (Figure 5) are in contrast to the dose dependence observed (Figure 4b).

The well-separated Si and Au grain growth curves (Figure 4b) cannot be explained by only considering the damage energy. One may argue that the cascade damage produced from Si and Au ions may be different, and therefore, contribute to grain growth differently. The recoil spectra from 3 MeV Au and 1 MeV Si ions are compared (Figure 6) to evaluate possible difference of energy transfer from collision events. While a slight higher probability for higher-energy recoils exists for 3 MeV Au, the energy distribution of the majority recoils produced from both ions has relatively low energies,  $< \sim 300$  eV, with very similar probability distribution (Figure 6). Moreover, an effective damage diameter of  $\sim 10$  nm is estimated for both ions (Figure 5c and f), and no significant difference is observed. Although the large numbers of defects resulting from atomic displacement events contribute to fast grain growth, the results (Figures 4-6) show that displacement damage is not the only contribution, and electron energy loss may play an important role.

### 3.4 Dependence on total energy loss

The significant transfer of energy to the electronic structure in the current study (Table 1) creates energetic electrons that produce a cascade of electron collisions on the electronic structure. A larger number of electron-hole pairs are produced, atomic bonds may be broken, atomic mobility may be enhanced, and electrons and holes may be trapped. These electronic excitation effects can significantly influence the kinetics of atomic processes in ceramics under irradiation, including damage recovery<sup>[38,39]</sup> or enhanced damage formation.<sup>[40]</sup> However, most of the energy transferred to electrons is dissipated locally (in less than one picosecond) in an inelastic thermal spike via electronic-phonon coupling,<sup>[41]</sup> and as noted above, inelastic thermal spikes in CeO<sub>2</sub> contribute additively to the production of defects and

disorder.<sup>[36,37]</sup> As a result, the contribution of electron energy loss may not be negligible. Radiation effects from energetic ions must be understood not only in terms of atomic collision cascades, but also in terms of the effects of the localized electronic energy deposition. Although the physics behind the processes of damage production within low and high energy regimes is fairly well understood, how materials respond to energy deposition to both electronic and atomic structures in the transition regime remains unclear. For MeV ions, the contribution of both nuclear and electronic energy loss are significant. Contrary to conventional understanding that atomic collisions and electronic excitation are two isolated and separate processes, this opens up the possibility that both nuclear and electronic energy deposition might produce effects that are competitive (damage annihilation), additive (the sum of the two components), or synergistic (enhanced damage production that is larger than the sum of the two).

Defect dynamics and self-healing mechanisms are complex in metallic systems and even more challenging in ceramics because of the significant variation in material properties, structure-types, and chemical composition. To investigate the distinct but coupled dynamics of electronic and atomic processes, the response of nanocrystalline cubic ZrO<sub>2</sub> films was investigated under 3 and 12 MeV Au irradiations. With increase in ion energy from 3 to 12 MeV, the damage energy decreases to half, and the electron energy loss increases nearly 30% (Table 1). To confirm that the damage energy is not the only driving force for the grain growth, the Au-irradiation induced grain growth was analyzed as a function of displacement damage in dpa (Figure 7). Since both cases are Au irradiations, microstructure modification from collision cascades and their impact to grain growth should be comparable. If displacement damage were to be the only dominate driving force, the grain growth should be less efficient under 12 MeV Au irradiation than that under the 3 MeV Au irradiation due to the lower nuclear energy loss. The slightly larger grain growth under the same dose observed for the 12 MeV irradiation (Figure 7) confirms an important contribution from the electron energy deposition to the overall grain growth.

The integrated effect from energy deposited to the electronic and atomic structures is evident from the grain growth in nanocrystalline CeO<sub>2</sub> and ZrO<sub>2</sub> under Si and Au ions. The irradiation-induced grain growth in CeO<sub>2</sub> under both Si and Au irradiations is plotted as a function of the total energy

deposition (Figure 8). The same energy dependence from both the Si and Au data indicates that both the damage energy and the total electronic energy loss contribute to the overall grain growth. While the separate effects from these two different energy deposition pathways are subject to future investigation, an additive effect is clearly evident. In  $\text{ZrO}_2$ , a similar dependence of grain growth versus total energy deposition can also be observed for 3 and 12 MeV Au irradiation (Figure 8), which further confirms the additive effects on grain growth from the energy deposited to the electronic and atomic structures. In the current study, the electron energy loss varies from 1.3 to 4.9 keV/nm and the nuclear energy loss from 0.12 to 3.1 keV/nm, with the total energy loss ranging from 1.4 to 6.9 keV/nm (Table 1). Within this energy region, the ratio of initial ion energy transfer to the electronic and atomic structures ranges from 1.3:1 to 3.3:1 for Au ions and is 12:1 for the Si ions (Table 1). It is, therefore, clear that both electron energy loss and damage energy are not negligible. An additive effect is shown as the grain growth can be simply described as a function of the total energy deposition in the films, competing or synergistic effects are not observed in nanocrystalline  $\text{CeO}_2$  and  $\text{ZrO}_2$ .

#### 4. Conclusion

In summary, the response of nanocrystalline  $\text{CeO}_2$  and  $\text{ZrO}_2$  to MeV ion irradiation has been investigated. Energy loss to both atomic collisions and electrons has significant impact on microstructure evolution and contributes to effective grain growth. By varying the amount of energy deposition into the electronic and atomic structures, an additive effect from both atomic collision cascades and electronic excitation on grain growth is observed that is well described as a function of total energy deposition in the nanocrystalline oxide films. Atomic level MD simulations provide insights on a disorder-driven grain growth mechanism that is triggered by the active interaction between irradiation-induced disorder and GBs. While a fast disorder-driven growth is dominant in small grains, it becomes less effective in larger grains as the defects tend to anneal rather than interact with the GBs. This study provides important evidence for understanding the effects of electronic energy loss on the kinetics of atomic processes, as well as data for validation of computational results. It has also clarified the controlling mechanisms of grain growth by minimizing the defect activity or concentration in small grains and by pinning GB

movement in the larger grains. This unraveling of mechanisms opens up new possibilities to better control grain sizes and to improve functionality of nanocrystalline materials.

### **Acknowledgements**

This work was supported as part of the Materials Science of Actinides, an Energy Frontier Research Center funded by the U.S. Department of Energy, Office of Science, Office of Basic Energy Sciences. A portion of research was performed at the UT-ORNL Ion Beam Materials Laboratory (IBML) located at the University of Tennessee, Knoxville and the Environmental Molecular Sciences Laboratory (EMSL), a national scientific user facility sponsored by the Department of Energy's Office of Biological and Environmental Research located at Pacific Northwest National Laboratory. The MD simulations were performed at the National Energy Research Scientific Computing Center at Lawrence Berkeley National Laboratory.

## References

- [1] C. Sun, H. Lia and L. Chen, Energy Environ. Sci., **2012**, 5, 8475.
- [2] M. Davenport, A. Rodriguez, K. J. Shea, Z. S. Siwy, Nano Letters **2009**, 9, 2125.
- [3] H. Mukaibo, L. P. Horne, D. Park, C.R.Martin, Small **2009**, 5, 2474.
- [4] J. N. David, A.L. Efros, S. C. Erwin, Science **2008**, 319, 1776.
- [5] F. Namavar, C. L. Cheung, R. F. Sabirianov, W.-N. Mei, X. C. Zeng, G. Wang, H. Haider, and K L. Garvin, Nano Letters **2008** 8, 988.
- [6] C. R. Martin, Z. Siwy, Science **2007**, 317, 331.
- [7] F. Ren, C.Z. Jiang, C. Liu, J.B. Wang, Phys. Rev. Lett. **2006**, 97, 165 501.
- [8] Z. Siwy, I. D. Kosinska, A. Fulinski, C. R. Martin Phys. Rev. Lett. **2005** 94, 048102.
- [9] H. Fan, K. Yang, D. M. Boye, T. Sigmon, K. J. Malloy, H. Xu, G. P. López, C. J. Brinker, Science **2004**, 304, 567.
- [10] W. J. Weber, A. Navrotsky, S. Stefanovsky, E. R. Vance, and E. Vernaz, MRS Bulletin **2009**, 34, 46-53.
- [11] L. V. Saraf, C. M. Wang, V. Shutthanandan, Y. Zhang, O. Marina, D. R. Baer, S. Thevuthasan, P. Nachimuthu and D. W. Lindle, Journal of Materials Research **2005**, 20, 1295.
- [12] Y. Zhang, W. Jiang, C. Wang, F. Namavar, P. D. Edmondson, Z. Zhu, F. Gao, J. Lian, W. J. Weber, Phys. Rev. B **2010**, 82(18) 184105.
- [13] K. E. Sickafus, H. Matzke, T. Hartmann, K. Yasuda, J. A. Valdez, P. C. Iii, M. Nastasi, and R. A. Verrall, J. Nucl. Mater. **1999**, 274, 66.
- [14] J. F. Ziegler, J. P. Biersack, and M. D. Ziegler, *The Stopping and Range of Ions in Solids* (SRIM Co. 2008), as well as the original book of by J. F. Ziegler, J. P. Biersack, and U. Littmark, (Pergamon, New York, 1985).
- [15] S. Moll, Y. Zhang, Z. Zhu, P. D. Edmondson, F. Namavar, and W. J. Weber, Nucl. Instrum. and Methods in Physics Research B, **2013**, 307, 93.
- [16] K. Jin, Y. Zhang, H. Xue, Z. Zhu, and W. J. Weber, Nucl. Instrum. and Methods in Physics Research B, **2013**, 307, 65.
- [17] K. Jin, Y. Zhang, Z. Zhu, D. A. Grove, H. Xue, J. Xue, and W. J. Weber, Journal of Applied Physics, **2014**, 115, 044903.
- [18] Y. Zhang, I-T. Bae, K. Sun, C. Wang, M. Ishimaru, Z. Zhu, W. Jiang, and W.J. Weber, Journal of Applied Physics, **2009**, 105, 104901.
- [19] K. Yasunaga, K. Yasuda, S. Matsumura, T. Sonoda, Nucl. Instru. and Meth. B **2008**, 266 2877.
- [20] A. Guglielmetti, A. Chartier, L. van Brutzel, J.-P. Crocombette, K. Yasuda, C. Meis, S. Matsumura, Nucl. Instru. and Meth. B **2008**, 266, 5120.
- [21] Handbook of Modern Ion Beam Materials Analysis: Appendices (2nd Edition) by Michael Anthony Nastasi, Yongqiang Wang. Materials Research Society, ISBN-10: 160511216X; ISBN-13: 9781605112169, Page 104.
- [22] D. S. Aidhy, Y. Zhang, and W.J. Weber, under consideration, Scripta Materialia, 2014.
- [23] A. Gotte, D. Spangberg, K. Hermansson, and M. Baudin, Solid State Ionics **2007**, 178, 1421.
- [24] H. Xu, R. K. Behera, Y. Wang, F. Ebrahimi, S. B. Sinnott, E. D. Wachsman, and S. R. Phillpot, Solid State Ionics **2010**, 181, 551.
- [25] D. S. Aidhy, D. Wolf, and A. El-Azab, Scripta Mater **2011**, 65, 867.
- [26] D. Wolf, P. Keblinski, S. R. Phillpot, and J. Eggebrecht, Journal of Chemical Physics **1999**, 110, 8254..
- [27] A. Okabe, B. Boots, and K. Sugihara, *Spatial tessellations: concepts and applications of voronoi diagrams* (Wiley, Chichester, 1992)
- [28] P. D. Edmondson, Y. Zhang, S. Moll, F. Namavar, and W. J. Weber, Acta Materialia **2012**, 60, 5408-5416.

- [29] A. V. Krasheninnikov and K. Nordlund, *J. Appl. Phys. (Applied Physics Reviews)*, **2010**, 107, 071301.
- [30] Y. Zhang, P.D. Edmondson, T. Varga, S. Moll, F. Namavar, C. Lan and W.J. Weber, *Physical Chemistry Chemical Physics*, **2011**, 13, 11946.
- [31] J. Lian, J. Zhang, F. Namavar, Y. Zhang, F. Lu, H. Haider, K. Garvin, W. J. Weber and R. C. Ewing, *Nanotechnology*, **2009**, 20, 245303.
- [32] D. Kaoumi, A. T. Motta, R. C. Birtcher, *J. Appl. Phys.* **2008**, 104, 073525.
- [33] M. Hillert, *Acta Metall.* **1965**, 13, 227.
- [34] J. Jagielski, Lionel Thomé, *Appl Phys A* **2009**, 97, 147.
- [35] K. Yasuda, M. Etoh, K. Sawada, T. Yamamoto, K. Yasunaga, S. Matsumura, N. Ishikawa, *Nucl. Instru. and Meth. B*, **2013**, 314, 185.
- [36] N. Ishikawa, K. Takegahara, *Nucl. Instru. and Meth. B*, **2012**, 272, 227.
- [37] Y. Sasajima, N. Ajima, T. Osada, N. Ishikawa, A. Iwase, *Nucl. Instru. and Meth. B*, **2013**, 314, 202.
- [38] L. Thomé, A. Debelle, F. Garrido, P. Trocellier, Y. Serruys, G. Velisa, and S. Miro, *Appl. Phys. Lett.* **2013**, 102, 141906.
- [39] Y. Zhang, T. Varga, M. Ishimaru, P.D. Edmondson, H. Xue, P. Liu, S. Moll, F. Namavar, C. Hardiman, S. Shannon, and W.J. Weber, *Nucl. Instru. and Meth. B*, **2013**, 10.1016/j.nimb.2013.10.095.
- [40] L. Thomé, A. Debelle, F. Garrido, S. Mylonas, B. Décamps, C. Bachelet, G. Sattonnay, S. Moll, S. Pellegrino, S. Miro, P. Trocellier, Y. Serruys, G. Velisa, C. Grygiel, I. Monnet, M. Toulemonde, P. Simon, J. Jagielski, I. Jozwik-Biala, L. Nowicki, M. Behar, W.J. Weber, Y. Zhang, M. Backman, K. Nordlund, F. Djurabekova, *Nucl. Instru. and Meth. B*, **2013**, 307, 43.
- [41] J. Zhang, M.Lang, R. C. Ewing, R. Devanathan, W. J. Weber, M. Toulemonde, *J. Mater. Res.*, **2010**, 25, 1344

TABLE 1: Ion irradiation parameters and SRIM predicted energy loss values.  $E_{\text{irr}}$  is the ion energy impinging on the surface of the oxide films.  $\Delta E_{\text{ele}}$  and  $\Delta E_{\text{nucl}}$  are the average values of the electronic and nuclear energy loss over the 300 nm and 450 nm film thickness for  $\text{CeO}_2$  and  $\text{ZrO}_2$ , respectively.  $\Delta E_{\text{ele-E}}$  and  $\Delta E_{\text{dam-E}}$  are the average values of electron energy loss (total energy loss to the target electrons from both ion and energetic recoils) and damage energy (total energy consumed in elastic collision events between atoms).  $\Delta E_{\text{total}}$  is the sum of the  $\Delta E_{\text{ele}}$  and  $\Delta E_{\text{nucl}}$  (the same as the sum of  $\Delta E_{\text{ele-E}}$  and  $\Delta E_{\text{dam-E}}$ ). The ratio of  $\Delta E_{\text{ele-E}}$  to  $\Delta E_{\text{dam-E}}$  is also included.

<i>Ion</i>	$E_{\text{irr}}$ (MeV)	$\Delta E_{\text{ele}}$ (keV/nm)	$\Delta E_{\text{nucl}}$ (keV/nm)	$\Delta E_{\text{ele-E}}$ (keV/nm)	$\Delta E_{\text{dam-E}}$ (keV/nm)	$\Delta E_{\text{total}}$ (keV/nm)	<i>Ratio</i>
Si in $\text{CeO}_2$	1.0	1.26	0.17	1.32	0.12	1.43	12:1
Au in $\text{CeO}_2$	3.0	1.97	3.75	3.63	2.09	5.72	1.8:1
Au in $\text{ZrO}_2$	3.0	2.59	4.33	3.85	3.07	6.92	1.3:1
Au in $\text{ZrO}_2$	12.0	4.02	2.31	4.86	1.47	6.33	3.3:1

### Figure Captions

**Figure 1** (Color online) GIXRD spectra for the as-deposited CeO<sub>2</sub> film and the films irradiated by 1 MeV Si to ion fluences of  $6.36 \times 10^{15} \text{ cm}^{-2}$  (1.4 dpa) and  $3.49 \times 10^{16} \text{ cm}^{-2}$  (7.8 dpa). Detailed comparison of the (111) peaks is shown as the inset. The dashed arrows have the same length as the peak width of the as-deposited film, and are located at the half maximum of all three peaks to show the width change upon irradiations.

**Figure 2** (Color online) (a) High-resolution TEM image of (a) the as-deposited CeO<sub>2</sub> nanocrystalline film and the films irradiated by 3 MeV Au at (b) 160 K to  $1.04 \times 10^{14} \text{ cm}^{-2}$  (~0.34 dpa) and at (c) 300 K to  $1.0 \times 10^{14} \text{ cm}^{-2}$  (~ 0.33 dpa). The SAED patterns are included as inset in the corresponding TEM images. The GIXRD results shown in (d) indicate the increase of grain size as a function of ion fluence at both irradiation temperatures.

**Figure 3** (Color online) Atomistic simulations of disorder-driven grain growth mechanism in nanocrystalline CeO<sub>2</sub> film. The size of the central grain shown in (a) and (e) is 4.5 nm and 6.5 nm, respectively. Both grains contain the same number of defects with the same local defect density. The time-dependent evolution is shown on the top (smaller grain) and bottom (larger grain) images, respectively. The corresponding time stamps are labeled in the corresponding images.

**Figure 4** (Color online) Grain growth of the nanocrystalline CeO<sub>2</sub> films under Si and Au room temperature irradiation, (a) as a function of ion fluence and (b) as a function of ion dose. The fitting uncertainty of the GIXRD spectra is indicated as the error bars, equivalent to the size of the symbols. The uncertainty in size determination is typically smaller than 2 nm, as shown by the two Si data points at ion fluence of  $3.49 \times 10^{16} \text{ cm}^{-2}$  or ~7.8 dpa in the two plots.

**Figure 5** (Color online) Collision plots from the SRIM detailed calculation with full damage cascades for 1000 ions penetrate a 300 nm CeO<sub>2</sub> film, (a)-(c) for 3 MeV Au ions, and (d)-(f) for 1 MeV Si ions. The plots contain all the ion-target atom collisions.

**Figure 6** Recoil energy spectra initiated by (a) 3 MeV Au and (b) 1 MeV Si ions through a 300 nm CeO<sub>2</sub> film showing the probability of recoils as a function of their energy.

**Figure 7** (Color online) Grain growth of nanocrystalline ZrO<sub>2</sub> as a function of ion dose under 3 and 12 MeV Au irradiations. The lines are curve fit to guide the eye.

**Figure 8** (Color online) Irradiation-induced grain growths of the nanocrystalline CeO<sub>2</sub> films under 1 MeV Si and 3 MeV Au irradiations and the nanocrystalline ZrO<sub>2</sub> films under 3 and 12 MeV Au irradiations as a function of total energy deposition in both (a) linear and (b) logarithmic scales. The uncertainty of fitting uncertainty of the GIXRD spectra is indicated as the error bars, equivalent to the size of the symbols. The uncertainty in size determination is typically smaller than 2 nm.

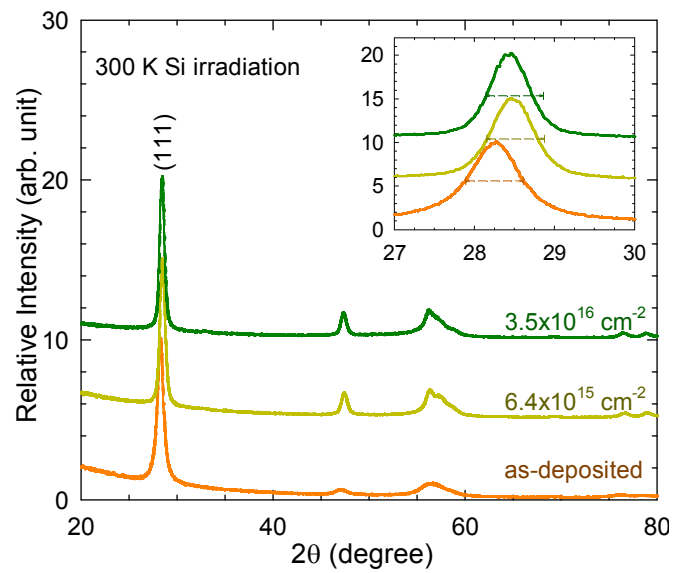


Fig. 1

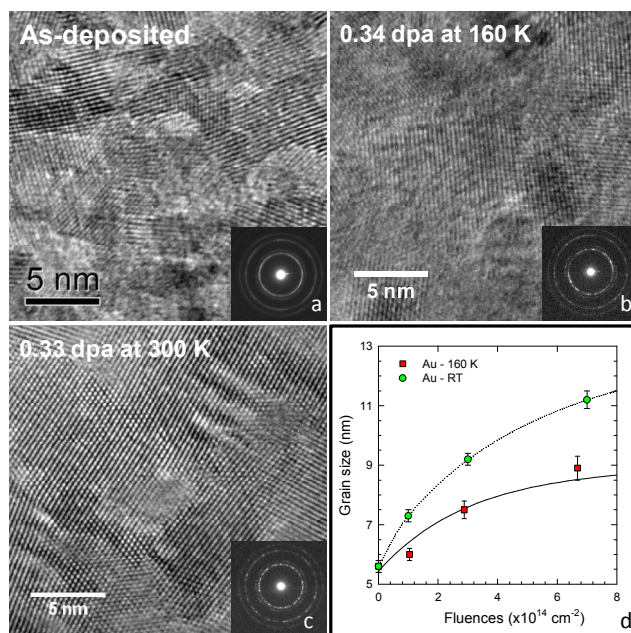


Fig. 2

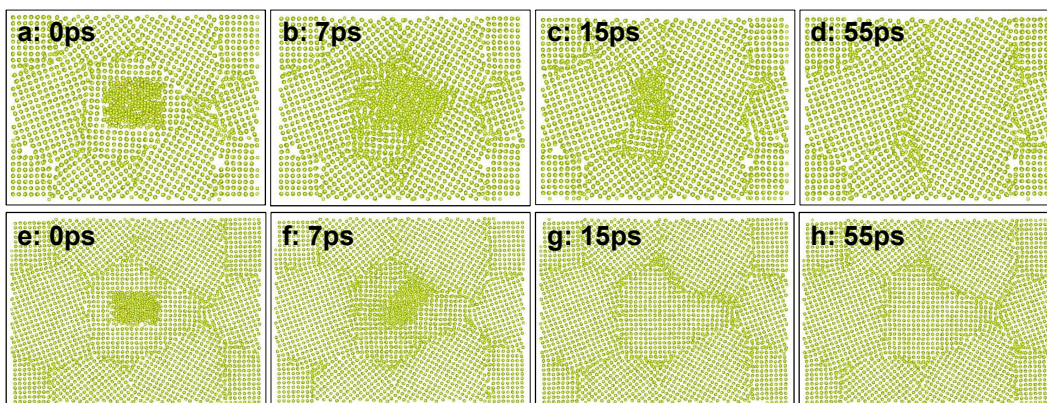


Fig. 3

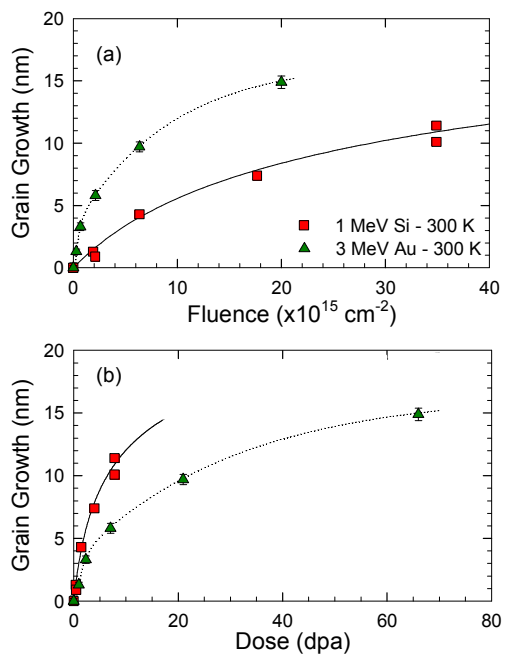


Fig. 4

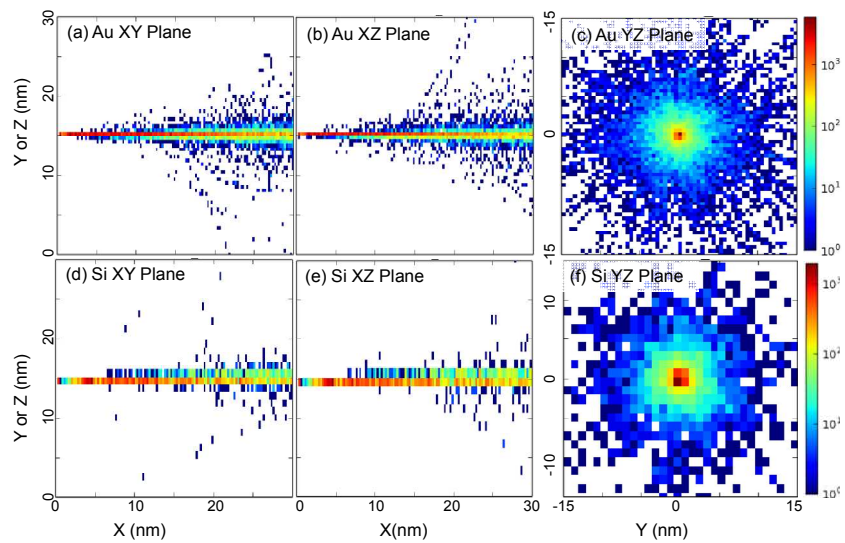


Fig. 5

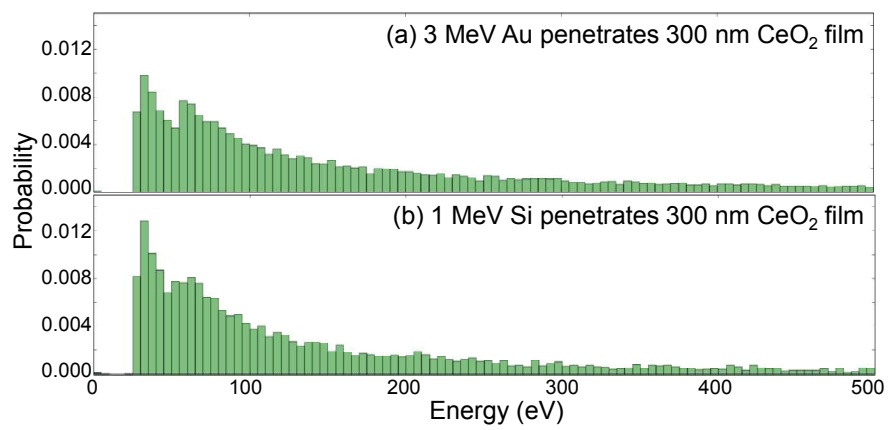


Fig. 6

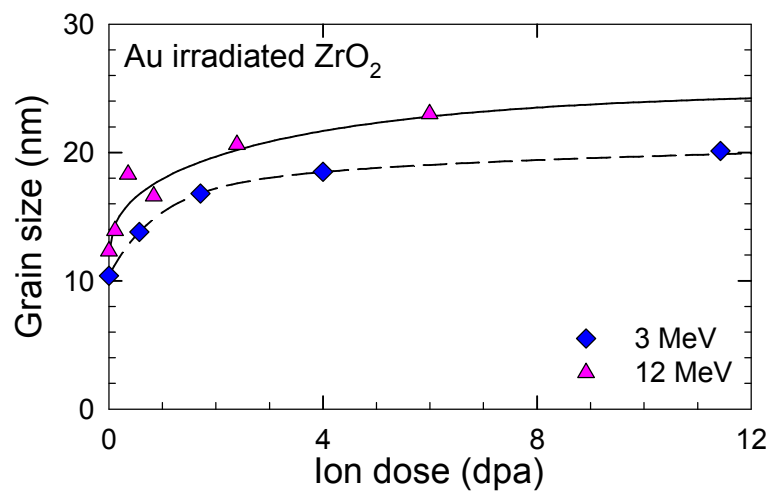


Fig. 7

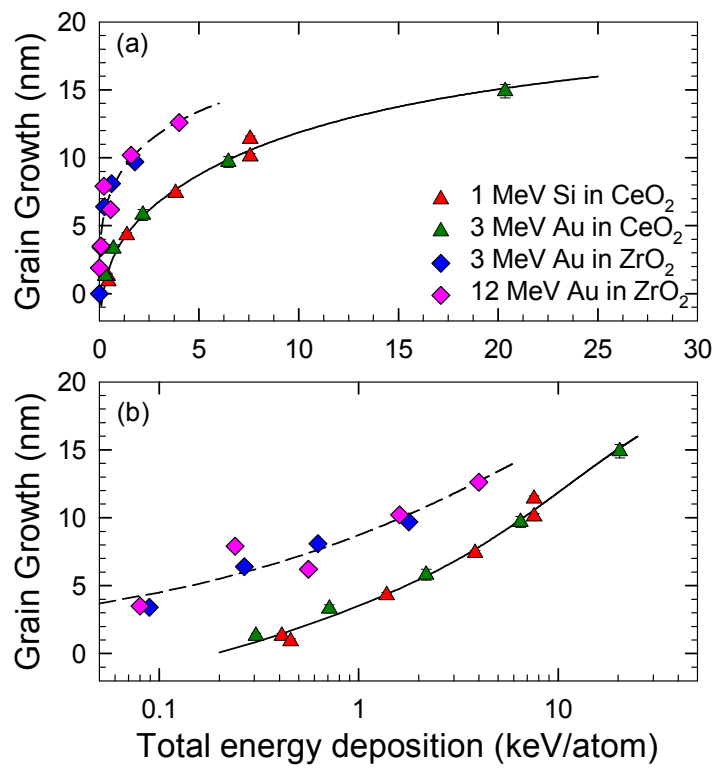


Fig. 8